

MARSIS: Mars Advanced Radar for Subsurface and Ionospheric Sounding

J.J. Plaut¹, G. Picardi², T.W. Watters³, D.A. Gurnett⁴ and the MARSIS Science Team

¹ *Jet Propulsion Laboratory, California Institute of Technology, Pasadena, CA 91109, USA*

Email: plaut@jpl.nasa.gov

² *Infocom Department, 'La Sapienza' University of Rome, I-00184 Rome, Italy*

³ *Center for Earth and Planetary Studies, National Air and Space Museum, Smithsonian Institution, Washington, DC 20560, USA*

⁴ *Department of Physics and Astronomy, University of Iowa, Iowa City, IA 52242, USA*

We report the findings of MARSIS from the first several months of its science operations phase. Subsurface soundings were used to probe the north polar layered deposits to their base, up to 1.8 km deep. The base of the south polar layered deposits was mapped, and the volume of the deposits was measured. Radar penetration was observed in the equatorial Medusae Fossae formation, indicating the presence of low-density material that may include water ice. In the ionospheric sounding mode, several types of echo were observed, ranging from vertical echoes caused by specular reflection from the horizontally stratified ionosphere, to a wide variety of oblique and diffuse echoes. Echoes at the electron plasma frequency and the cyclotron period provide measurements of the local electron density and magnetic field strength.

The Mars Advanced Radar for Subsurface and Ionospheric Sounding (MARSIS) is the first radar to collect data from Mars orbit. MARSIS is a multi-frequency synthetic aperture orbital sounding radar (Picardi et al., 2004) that operates in two modes, subsurface sounding and ionospheric sounding. In both modes, MARSIS acquires data in the conventional fashion of a radar, in which pulses of electromagnetic radio waves are transmitted, interact with a target, and the echoes are received and recorded by the instrument. MARSIS differs from most orbital radars in the frequencies of the radar signal. MARSIS operates in the range 0.1–5.5 MHz, which corresponds to wavelengths of tens to hundreds of metres. These long wavelengths were chosen, in the case of the subsurface sounder, to maximise the penetration of the signal into the subsurface of Mars. In the case of the ionospheric sounder, the selected frequencies are in the range where some waves reflect from the topside of the ionosphere, depending on the electron plasma frequency, while others penetrate through to be reflected at the surface or subsurface.

The primary goal of the MARSIS subsurface experiment is to detect material discontinuities in the subsurface of Mars in order to understand the distribution of water, both solid and liquid, in the upper crust. The experiment is also probing for other discontinuities in the subsurface, related to geological units and structures. Finally, the subsurface mode obtains information in its surface echoes on the electromagnetic, topographic and roughness properties of the Mars surface. The goals of the ionospheric sounding experiment are to characterise the upper portions of the atmosphere (the ionosphere) and its interactions with solar radiation and particles.

1. Introduction

2. MARSIS Instrument and Data

MARSIS data are collected when the elliptical orbit of Mars Express brings the spacecraft to an altitude of 250–1400 km above the surface; this condition is met during about 45 min of each 6.7 h orbit. Subsurface sounding data may be collected when the altitude is below 1000 km. In the subsurface modes, MARSIS operates in four frequency bands between 1.3 and 5.5 MHz, with a 1 MHz instantaneous bandwidth that provides free-space range resolution of approximately 150 m. Lateral spatial resolution depends on surface roughness characteristics, but for most Mars surfaces the cross-track footprint is 10–30 km and the along-track footprint, narrowed by onboard synthetic aperture processing, is 5–10 km. Peak transmitted power out of the 40 m dipole antenna is ~10 W. Coherent azimuth sums are performed onboard on ~100 pulses taken at a pulse repetition frequency of 127 Hz, with a resulting signal-to-noise ratio for a typical Mars surface of 30–50 dB. Ionospheric soundings are carried out by transmitting a short pulse at a frequency, and then measuring the time delay, for the echo to return. The time delay is measured as a function of frequency by sequentially stepping the transmission frequency over the frequency range of interest.

MARSIS's sounding signals will not reach the surface when the ionospheric plasma frequency is close to or above the sounding frequency. The frequency bands were therefore chosen to minimise distortion by the ionosphere; typically bands centred at 1.8 and 3.0 MHz were used on the nightside, and bands centred at 4.0 and 5.0 MHz were used on the dayside. Data were collected in a MARSIS subsurface sounding mode which returns complex spectra of summed pulses from three synthetic aperture channels for each of two frequency bands. Once received on the ground, the spectra are transformed from frequency domain to time domain. Processing includes a correction for phase distortion in the ionosphere (Safaenili et al., 2003).

3. North Polar Layered Deposits

Surrounding the north pole of Mars are layered deposits (NPLD) that consist mainly of an upper stratigraphic unit, thought to be dominated by water ice, which is typically finely layered due to varying fractions of included dust (Thomas et al., 1992). A second, lower unit that is absent at some longitudes contains a significant sand component that is likely ice-cemented (Byrne & Murray, 2002). Previous compositional and stratigraphic interpretations of these deposits have been based on imaging, spectral, thermal and topographic measurements. In an early MARSIS orbit, 1855, the NPLD were briefly observed in the longitude range 10°–40°E from altitudes of 800–900 km, on the nightside, in the frequency bands centred at 3.0 and 5.0 MHz. The radargrams show the surface reflection splitting into a pair of strong reflectors as the ground track passes from the northern plains onto the layered deposits (Fig. 1). The lower reflector extends to the end of the track, where it occurs at a time delay of 21 μ s relative to the surface reflection. Interpretation of radar sounding data requires discriminating between signals arising from subsurface interfaces and those coming from surface topographic features at the same time delay (surface 'clutter'). A high-fidelity model of the expected contribution of off-nadir topographic clutter, based on gridded Mars Orbiter Laser Altimeter (MOLA) data (Smith et al., 1999; Nouvel et al., 2004), shows no visible surface topographic feature that explains this reflector pair. Hence we conclude that the second reflector is a subsurface ('basal') reflector.

The time delay to and the relative echo strength of the basal reflector are consistent with the overlying material (away from the boundary) having a dielectric constant and loss tangent similar to that of fairly pure water ice. This is in accord with the absence of the lower, sandy stratigraphic unit in this region of the NPLD, as inferred from its lack of exposure in troughs in the longitude range 290°–90° E. The basal reflector time delay increases, with respect to the surrounding plains, as it proceeds inward from the NPLD boundary (Fig. 1). This is due to the slower velocity of the NPLD material relative to the martian atmosphere (approximately free-space velocity). Converting time to distance using a dielectric constant of pure ice (~3) brings the maximum

basal reflector depth up to about the level of the plains; i.e. the depth to the reflector is approximately the height of the NPLD above its surroundings (about 1.8 km at the right edge in Fig. 1). Either this is a coincidence or the material in this region of the NPLD is dominated by ice sitting directly on the underlying plains material.

The wave attenuation properties strengthen the case for nearly pure ice. Among plausible geological materials, only pure or slightly dirty water ice has a sufficiently low value of loss tangent to explain the strength of the subsurface reflection observed. Simple two-layer modelling has been applied to estimate the loss tangent of the ~ 1.8 km NPLD layer. The two interfaces considered are one at the atmosphere/surface ice boundary and a second at the ice base at ~ 1.8 km depth. The MARSIS-measured ratio of the reflected power from these two interfaces at 5 MHz is approximately -10 dB. This ratio is consistent with an ice layer dielectric of 3, an underlying material dielectric of 4.5 (basaltic regolith) and an ice layer loss tangent which must be low, below 0.001 (conductivity $<10^{-6}$ Siemens/m). The low loss tangent of the 1.8 km thick ice layer gives rise to relatively low attenuation of MARSIS radar signals, thereby allowing the base to be easily detectable. Ice conductivity is temperature-dependent. The low loss and low conductivity of the ice indicate that it can not contain more than a trace (2%) of impurities, and suggest a bulk temperature below 240K. These observations are inconsistent with the presence of a melt zone at the base of the NPLD.

The NPLD will act as a load on the underlying elastic lithosphere and should cause a flexural/membrane downward deflection of the plains. In order to leave a residual deflection after the velocity conversion, the dielectric constant of the NPLD would have to be less than 3, which we deem unlikely. An elastic thickness in excess of 150 km would produce a deflection of 500 m or less, which is well within the resolution of our interface detection. Thus a very thick elastic lithosphere (and a low crust/upper mantle temperature gradient) is implied for the north polar region.

In a typical MARSIS observation over the SPLD (Fig. 2), the echo from the surface splits into two continuous traces as the spacecraft passes over the margin of the deposits. The surface trace follows a profile expected from MOLA topography. The bright lower trace occurs at a time delay consistent with a continuation of the surrounding surface topography beneath the SPLD, assuming a nominal value of refractive index of water ice. The lower interface is interpreted as the boundary between the base of the ice-rich SPLD materials and the predominantly lithic substrate. The interface is detected beneath most of the SPLD, although in places it becomes discontinuous, indistinct or absent. It is generally lower in backscatter intensity than the surface above it, but in places it appears equivalent to or brighter than the surface echo. Propagation of the signal in the SPLD medium can be described with a simple two-layer homogeneous model, using reflection and absorption coefficients appropriate for materials expected on Mars. As in the case of the NPLD, the strong return from the basal interface indicates very low attenuation values within the SPLD. Assuming ‘dirty’ water ice overlying a basaltic substrate, effective loss tangent values between 0.001 and 0.005 are obtained for the SPLD material. This corresponds to water ice with a dust contamination of 0–10%. The general behaviour of the surface and subsurface echoes over most of the SPLD is consistent with a composition of water ice that is relatively free of impurities overlying a typical martian regolith and crust.

An extended area of unexpectedly bright basal reflections occurs in an area between the thickest part of the SPLD (~ 3.7 km; see discussion of SPLD thickness below) and the nearby SPLD margin, from 310° to 0° E (Fig. 2). The returns are often brighter than the surface return, which is not expected for propagation through a lossy medium. While a strong contrast in dielectric constant at the base may be responsible, we deem it highly unlikely that liquid water (basal melting) causes the bright return, because it occurs below thin (as well as thick) sections of the SPLD that

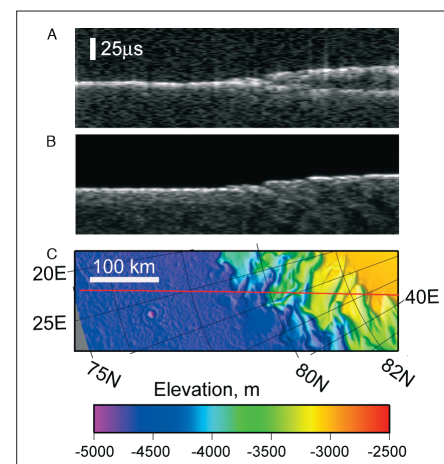
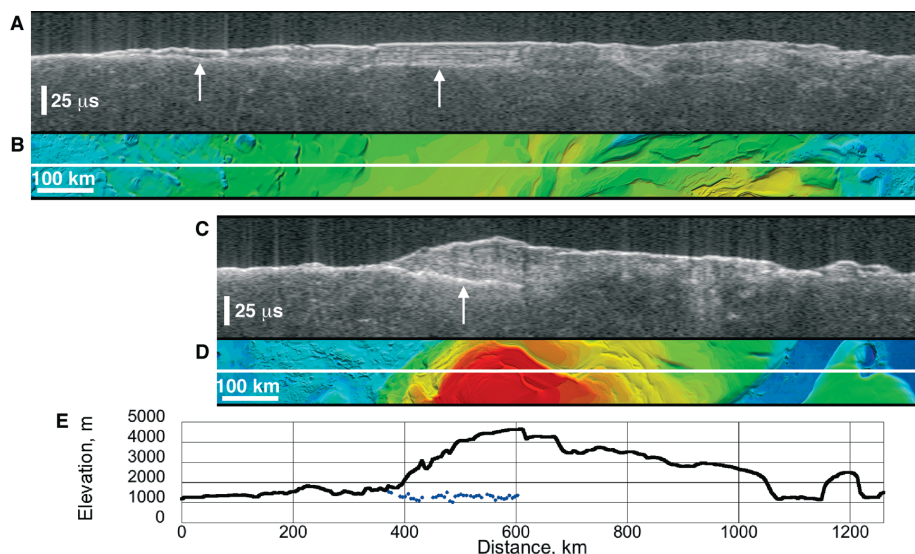


Fig. 1. (A) MARSIS data in radargram format for orbit 1855 as it crosses the margin of the north polar layered deposits. (B) Simulated MARSIS data if echoes are only from the surface (nadir and off-nadir clutter). (C) MOLA topography along the ground track (red line); elevation is relative to the mean planetary radius. MARSIS data at 5 MHz show a split of the strong return into two as the ground track reaches the NPLD (higher terrain to the right). Maximum time delay to the second reflector is 21 ms, equivalent to 1.8 km depth in water ice.

4. South Polar Layered Deposits (SPLD)

Fig. 2. (A) MARSIS data from orbit 2753 showing typical features of the SPLD. (B) MOLA topography along the ground track. The lower echo trace (arrows) is interpreted as the SPLD basal interface with the substrate. The basal reflector becomes indistinct right of centre. The central area shows multiple continuous bands internal to the SPLD, where the estimated SPLD thickness is 1.6 km. (C) MARSIS data from orbit 2682 showing a bright basal reflector (arrow). (D) MOLA topography along the ground track. The reflector extends from the margin of the SPLD (left of centre) to below a 3.5 km thick section of the SPLD. The basal reflector abruptly disappears for unknown reasons. (E) MOLA surface elevations (black line) and MARSIS measured basal elevations (blue symbols), assuming a refractive index of ice. The basal reflector is at a fairly constant elevation between 1000 and 1500 m. The apparent curvature of the reflector in (C) is an artefact of the time representation of the data. Vertical dimension in (A) and (C) is round-trip travel time. See Fig. 3 for the location of ground tracks and MOLA elevation scale.



are among the coldest places on the surface of Mars. The low attenuation is consistent with very low temperatures throughout the ice, further arguing against basal melting. Nevertheless, we cannot completely rule out unusual geothermal conditions or an exotic composition of the substrate in these anomalously bright areas.

A pattern of banding commonly occurs between the surface and basal interface traces in MARSIS radargrams of the SPLD (Fig. 2). The banding consists of bright continuous reflectors, sometimes hundreds of kilometres long, alternating with lower backscatter bands. The banding is certainly related to the layered structure of the SPLD, possibly due to contrasts in dust content or density, but the precise mechanism that creates the bands is unknown. The position and brightness of the bands sometimes varies with the frequency of the MARSIS observation, suggesting that the bands may be due to interference effects that depend on the relative scales of the radar wavelength and the internal layering of the SPLD.

Detection of the basal interface below most of the SPLD allows us to generate a map of the topography of this interface, and to provide new estimates of the thickness and volume of the SPLD. The methodology used is as follows. The time delay was measured between the peak of the surface reflection and the peak of the last bright continuous reflector, which is assumed to be the basal interface. Over 1800 points from 60 high-quality MARSIS orbits were used. The orbits were chosen to provide coverage that was sufficiently dense to generate medium resolution maps of basal topography and SPLD thickness. Data from two frequencies were evaluated for most points. All points were verified to be actual subsurface reflectors and not surface ‘clutter,’ using simulations of surface echoes based on MOLA topography. The vertical resolution of the data used was about 100 m in ice, with an estimated uncertainty on a given measurement less than 200 m. To convert time delay to depth we used the refractive index of pure ice with a real dielectric constant of 3. We could reasonably expect this estimate to be off by ± 0.5 , which translates into an additional error in our depth estimate of somewhat less than 10%. Figure 3 shows a map of the locations of the measured points.

To obtain a map of the basal interface, the MARSIS-measured elevations of the interface were combined with MOLA elevations along the margin of the SPLD unit as mapped by Tanaka & Kolb (2005), where the thickness of the unit is considered to be zero. The results of a ‘natural neighbour’ interpolation of these data are shown in Fig. 4. The map of the sub-SPLD topography is generally consistent with that expected from simple interpolation of MOLA data from the margins of the unit. The

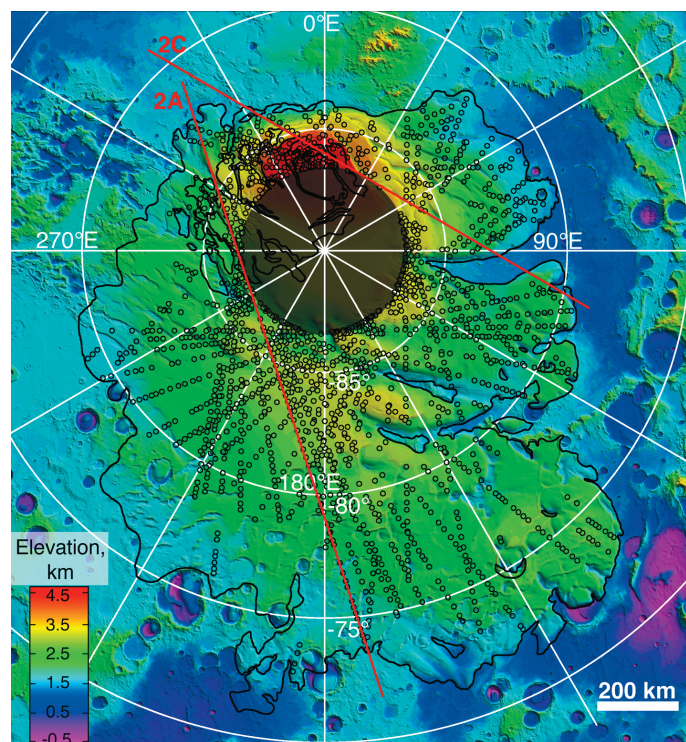


Fig. 3. Topography of the south polar region of Mars from MGS MOLA data, with locations of MARSIS measurements of the SPLD thickness shown as open circles. The SPLD unit mapped by Tanaka and Kolb (2005) is outlined in black. Red lines indicate ground tracks of orbits in Fig. 2. Apparent gaps in coverage are due to the lack of a discernible basal interface, and not to gaps in observations. No MARSIS data are available poleward of 87°S (dark circle in upper centre).

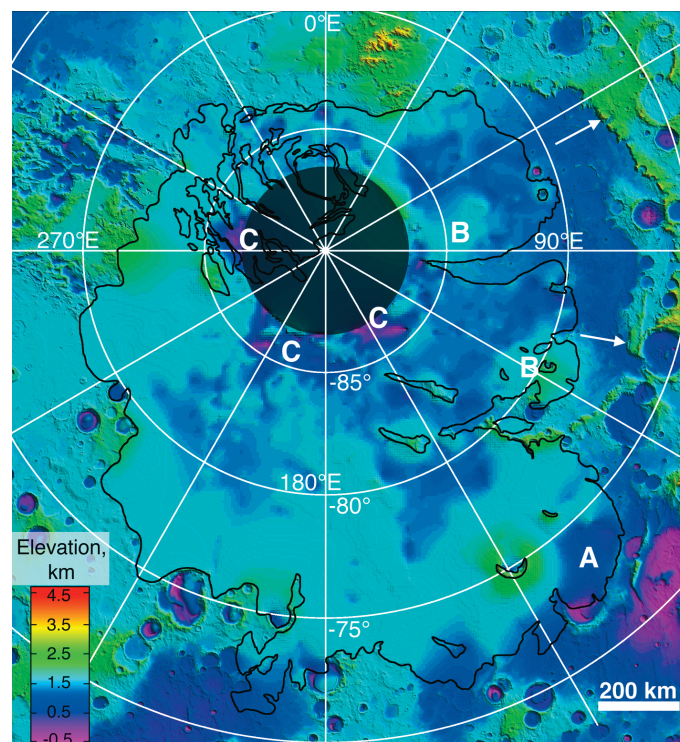
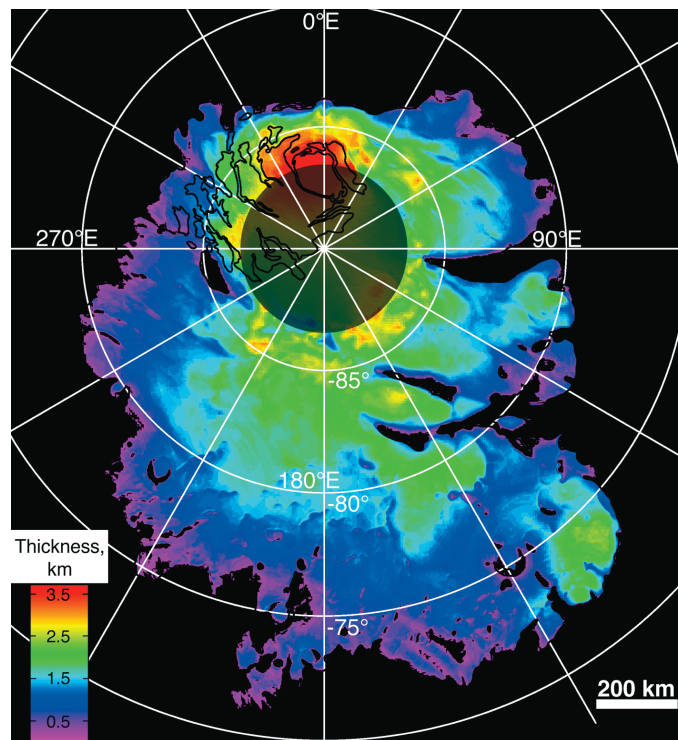


Fig. 4. Same as Fig. 3, with topography at the SPLD basal interface shown, based on MARSIS measurements of SPLD thickness. A indicates a depression below a distal SPLD lobe. B indicates relative highs within the remnant Prometheus basin (basin rim indicated with arrows). C indicates depressions in the near-polar region.

surface is typically low in relief, with broad areas of higher and lower topography. A pronounced low area is seen near the SPLD margin around 72°–74°S, 130°–145°E, and elevated regions within the remnant Prometheus impact basin are seen to continue below the SPLD at 78°–82°S, 100°–130°E and from 70°–90°E poleward of about 83°S. An unexpected feature of the basal topography is a series of depressions at the highest latitudes (84°–87°S). These occur discontinuously from longitudes 95° to 295°E. The depressions range in width from 50 to 200 km, and reach a depth of as much as 1 km below the surrounding sub-SPLD topography. The basal reflection within the depressions is typically dimmer than under the rest of the SPLD. This, and the position of the depressions in the near-polar areas suggest there may be processes unique to this sub-SPLD area. The depressions may be the result of differential compaction of mega-regolith in response to the SPLD load. Alternatively they may be a group of buried impact craters or other pre-existing topography such as the ~km-deep pits ('Cavi') in the nearby plains. On a regional scale, the basal interface is relatively flat. The lack of evidence of regional downwarping in response to the SPLD load suggests the elastic lithosphere in the south polar region is very thick (>150 km), as was inferred for the north polar region.

A thickness map of the SPLD was generated by subtracting the elevations of the interpolated basal topography from the high-resolution MOLA surface topography (Fig. 5). The distribution of SPLD thickness reflects the asymmetry of the south polar geology, with the thickest portions offset from the pole near 0°E, and the much more areally extensive but thinner portion centred near 180°E. The newly discovered

Fig. 5. Map of the SPLD thickness, based on MARSIS measurements and MOLA surface topography. An anomalous thick section appears in lower right (see A in Fig. 4). The thickest areas occur beneath the highest elevations of the SPLD (red areas near top), and in association with the near-polar depressions (see C in Fig. 4).



near-polar depressions show clearly as anomalously thick areas, as do several of the distal lobes. The maximum measured thickness is 3.7 ± 0.4 km, under the highest elevations of the SPLD near 0°E . Our estimate of the integrated volume of the entire SPLD is $1.6 \pm 0.2 \times 10^6$ km³. This translates to an equivalent global water layer thickness of 11 ± 1.4 m (assuming an SPLD composition of nearly pure ice), and is within the range estimated by previous workers using MOLA data alone (Smith et al., 2001). Knowledge of the basal topography now allows us to estimate the volume with a much smaller range of uncertainty.

MARSIS data do not allow us to distinguish a component of CO₂ ice in the SPLD material, but there is no corroborative evidence for such a component. Spectral and albedo observations of the surface of the SPLD indicate an optically thick lag of dust or rocky material, but this layer is ‘optically’ thin at MARSIS wavelengths. Similarly, MARSIS detects no difference in surface or subsurface echoes from areas covered by the residual (‘perennial’) CO₂-rich ice unit, consistent with recent analyses indicating it is a deposit no more than a few tens of metres thick (Byrne & Ingersoll, 2003).

5. Medusae Fossae Formation

Units of the Medusae Fossae formation (MFF) occur discontinuously at equatorial latitudes along the boundary of the hemispheric dichotomy from Amazonis to Elysium Planitiae ($\sim 130^\circ\text{--}240^\circ\text{E}$) (Scott & Tanaka, 1986; Greeley & Guest, 1987). The MFF may be among the youngest surficial deposits on Mars, unconformably overlying ancient Noachian heavily cratered highlands and young Amazonian lowlands (Bradley et al., 2002). The local topographic relief of the MFF units varies greatly, reaching a maximum of more than 3.5 km (Zimbelman et al., 1999; Hynek et al., 2003; Head & Kreslavsky, 2004). The morphology of the MFF units is complex and variable. Over large horizontal scales (tens of kilometres), the undulating hills of the MFF are relatively smooth (Fig. 6). At smaller scales, many of the MFF units are marked by systems of parallel ridges and grooves interpreted as yardangs (Fig. 7). Remnant yardangs and

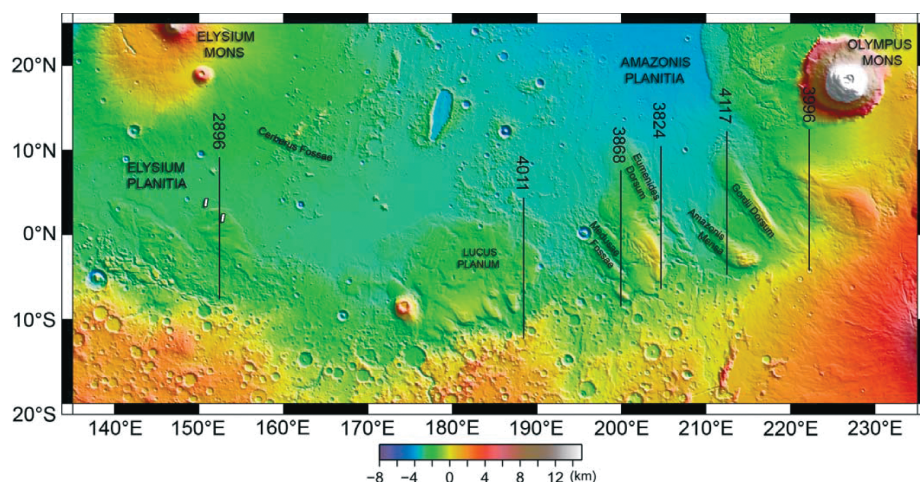


Fig. 6. The Medusae Fossae formation in Elysium and Amazonis Planitiae along the dichotomy boundary. The locations of MARSIS orbit tracks 2896, 4011, 3868, 3824, 4117 and 3996 are indicated by back lines (from left to right) overlaid on MOLA colour-coded shaded relief. The locations of Thermal Emission Imaging System (THEMIS) images shown in Fig. 7 are indicated by the small white rectangles.

outliers some distance from the thicker units suggest that MFF deposits once covered a larger area of the northern lowlands (Bradley et al., 2002) (Fig. 7a).

Layering is observed in the MFF deposits that varies in scale from coarse, indurated layers that cap weaker, more friable material to thin, pervasive layering. A variety of origins have been proposed for the MFF deposits. These include ignimbrite or volcanic ash deposits from now-buried vents (Scott & Tanaka, 1986; Greeley & Guest, 1987), aeolian deposits from materials weathered early in martian history (Scott and Tanaka, 1986), and deposits analogous to polar layered and circumpolar deposits formed either as a consequence of polar wandering (Schultz & Lutz, 1988) or during periods of high obliquity (Head and Kreslavsky, 2004). Units of the MFF are associated with the ‘Stealth’ region on Mars, so named because no echo is detected in Earth-based radar data (Muhleman et al., 1991). In MARSIS observations of the MFF deposits, subsurface echoes are detected that correspond to the basal interface between the MFF material and the underlying plains material.

We can characterise the thickness and electrical properties of the MFF deposits as a guide to their bulk porosity and/or ice fraction. MARSIS data obtained between March 2006 and April 2007 cover all the units of the MFF (Fig. 6). Radargrams show subsurface echoes, offset in time delay from the surface return, where the tracks cross the MFF (Fig. 8). The subsurface echoes generally parallel the surface return except near the margins where, in some cases, the subsurface and surface echoes converge (Fig. 8). The observed time delay in the radargrams is consistent with the expected depth to the interface between the MFF deposits and the underlying terrain. The westernmost MFF deposits form low-relief, undulating hills (Fig. 6) and overlie relatively young (Late Amazonian-aged) lowlands volcanic plains associated with Cerberus Fossae (Fig. 7a). The inferred elevation of the subsurface interface corresponds closely with the floor of a valley separating two hills where MFF material has been almost completely stripped away, nearly exposing the Cerberus plains (Fig. 7b and Fig. 8a). The MFF material that forms Lucus Planum is deposited on older (Hesperian-aged), lowlands knobby terrain (Fig. 6). The interface beneath the eastern flank of this unit is flat and largely continuous (Fig. 8b). The MFF material exposed in the pronounced valley of Medusae Fossae itself extends from the northern lowlands into the ancient heavily cratered (Noachian-aged) southern highlands, locally burying the dichotomy boundary and the cratered highlands (Fig. 6). A generally flat, continuous subsurface interface that extends for several hundred kilometres is separated in time delay from a shallower, discontinuous interface associated with a layer internal to the MFF deposits (Fig. 8c). The subsurface echo from the eastern flank of Eumenides Dorsum is more spread out in time delay but appears to delineate the north-downward slope of the buried dichotomy boundary (Fig. 8d).

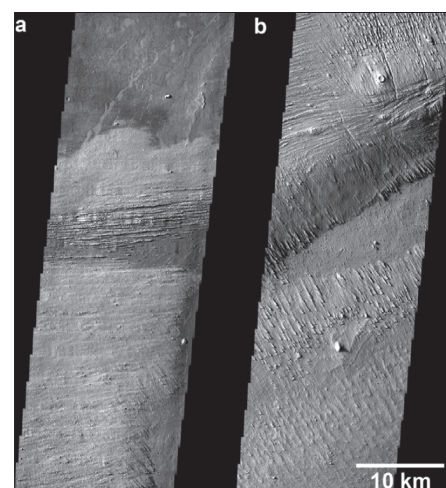


Fig. 7. High-resolution THEMIS images of the MFF material in Elysium Planitia. (a) THEMIS visible image (frame #V05275021) shows an outlier of MFF material that is being stripped, partially exposing the underlying lowlands plains. (b) THEMIS visible image (frame #V13163010) shows numerous yardangs and a valley stripped of MFF material. The locations of images (a) and (b) are to the left and right, respectively, of orbit track 2896 shown in Fig. 6.

Fig. 8. Radargrams showing MARSIS data for orbit 2896 (a), 4011 (b), 3868 (c), 3824 (d), 4117 (e), and 3996 (f). Echoes are plotted in time delay versus position along the orbit. The subsurface echoes are offset in time delay from the surface echo and are interpreted to be nadir reflections from the interface between the MFF deposits and the lowland plains material. The peak surface return is corrected to agree with the MOLA topography along the orbit track. The radargrams are resampled to a uniform along-track length of ~ 1000 km. All the orbits are ascending except for orbit 2896.

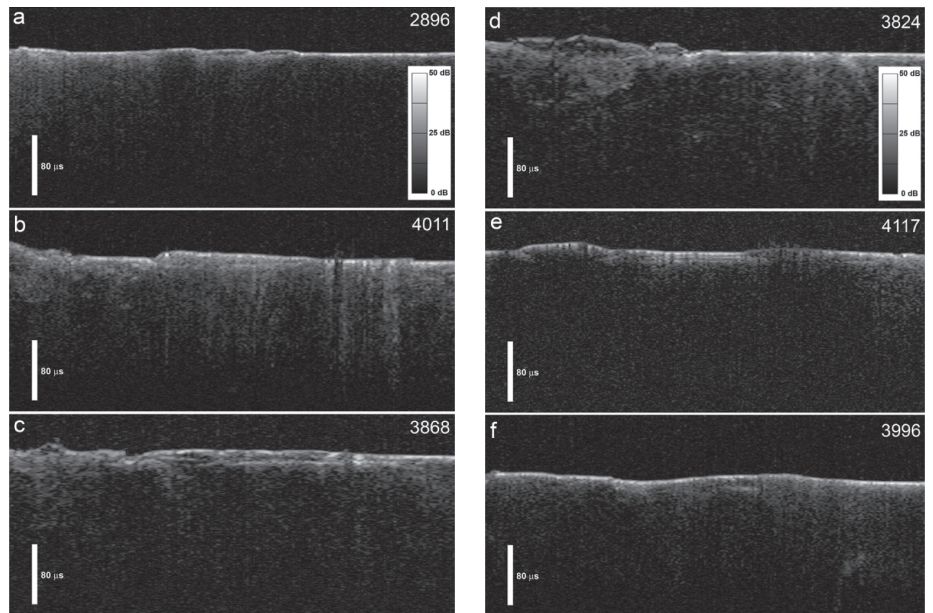
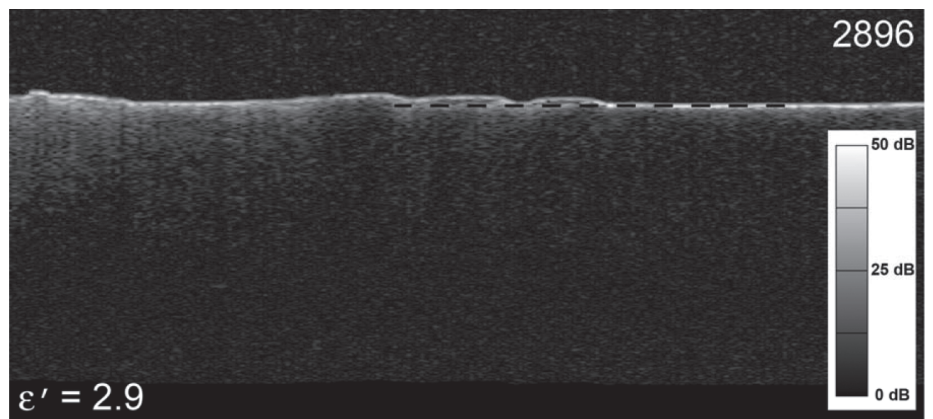


Fig. 9. Radargram showing MARSIS data for orbit 2896 converted to depth using a dielectric constant $\epsilon' = 2.9$ for the MFF material. The dashed black line shows the projection of the lowland plains beneath the MFF deposits. There is good agreement between the basal reflector and the projection of the exposed surrounding plains (compare with Fig. 8a).



MFF material overlying Amazonian-period volcanic plains forms the prominent ridges of Amazonis Mensa and Gordii Dorsum (Fig. 6). There are two parallel subsurface echoes from the valley between the ridges (Fig. 8e) that correspond to the base of the MFF material and an internal dielectric horizon. The discontinuous subsurface echoes associated with the northern tip of Gordii Dorsum correlate in time delay with the basal echo from the valley floor (Fig. 8e, far right in radargram). The easternmost MFF deposits overlie the dichotomy boundary and Amazonian volcanic plains of Olympus Mons and the Tharsis Montes and narrow northwestward into a ridge (Fig. 6). A discontinuous subsurface reflection from beneath the western part of the ridge suggests a flat basal interface (Fig. 8f). Previous analyses suggested that some MFF units are draped over pre-existing topographic rises in the lowlands (Sakimoto et al., 1999).

The subsurface interfaces revealed by MARSIS suggest that MFF materials are deposited on generally planar materials in the northern lowlands and the downward slope of the dichotomy boundary (Fig. 8). MARSIS data support estimates of the total volume of MFF material calculated using apparent base-level elevations in the lowlands. These estimates range from 1.4×10^6 km³ (Lanagan et al., 2001) to 1.9×10^6 km³ (Hynek et al., 2003). MARSIS observations provide an opportunity

to evaluate the electrical properties of the MFF where the material is deposited on lowlands plains that are exposed nearby (Fig. 7a). The observed time delays in the MFF deposits correspond to a bulk real dielectric constant ϵ' of $\sim 2.9 \pm 0.4$, based on the projection of the surrounding plains beneath the material (Fig. 9). A variation in ϵ' of 2.5 to 3.3 does not result in a large range in the radar-predicted thickness because h is a function of the square root of ϵ' . The dielectric properties of a material are related to its density and composition. The real part of the dielectric constant is modulated strongly by density. The imaginary component of the dielectric constant ϵ'' and the loss tangent are strongly influenced by target composition. Radar losses due to attenuation in the deposits were estimated using the method outlined in Porcello et al. (1974). At 4 MHz centre frequency (band 3), we obtain losses of $\sim 0.0048 \pm 0.0024$ dB/m. For ϵ' of 2.9 and a centre frequency of 4 MHz, these losses correspond to a range in loss tangent of ~ 0.002 to 0.006. MARSIS studies of the PLD (Picardi et al., 2005; Plaut et al., 2007) suggest a value for ϵ' of about 3, consistent with pure water ice, based on the agreement between the inferred depth of the basal interface and the projection of the surrounding surface. The loss tangent of the PLD is estimated to range from <0.001 to 0.005. Our analysis suggests a similar real dielectric constant (2.5–3.3) and a comparably low range of loss tangent (0.002–0.006) for the MFF materials. The loss tangents derived for the MFF deposits are below the range measured for terrestrial volcanic materials but are comparable to some low-titanium lunar materials (Carrier et al., 1991).

Thus, our first-order estimates of the dielectric losses span a range that includes some dry, unconsolidated geological materials and mixtures of pure water ice and sediment. The real dielectric constant of the MFF and PLD deposits is also low relative to the behaviour of compacted rock-derived materials. A maximum ϵ' of 3.3 corresponds to an average density of about ~ 1.8 g/cm³, which is low for the expected self-compaction of 0.5–2.5 km of a dry geological material. There are two plausible interpretations of these observations. The first is that the MFF material is poorly consolidated and comprised of non-ice material with low dielectric loss. If the MFF material is an ice-poor ash or aeolian deposit, it must have an unusually high porosity and low bulk density at depths up to 2.5 km to account for the estimated values of ϵ' . MFF deposits with a depth-averaged bulk density >1.9 g/cm³ will have an ϵ' value outside the measured range. The second possibility is that the MFF material is ice-rich, with a non-ice component of higher real dielectric constant and loss tangent (ice present as a minor component within a matrix of $\epsilon' = 6$ does not match the observed properties).

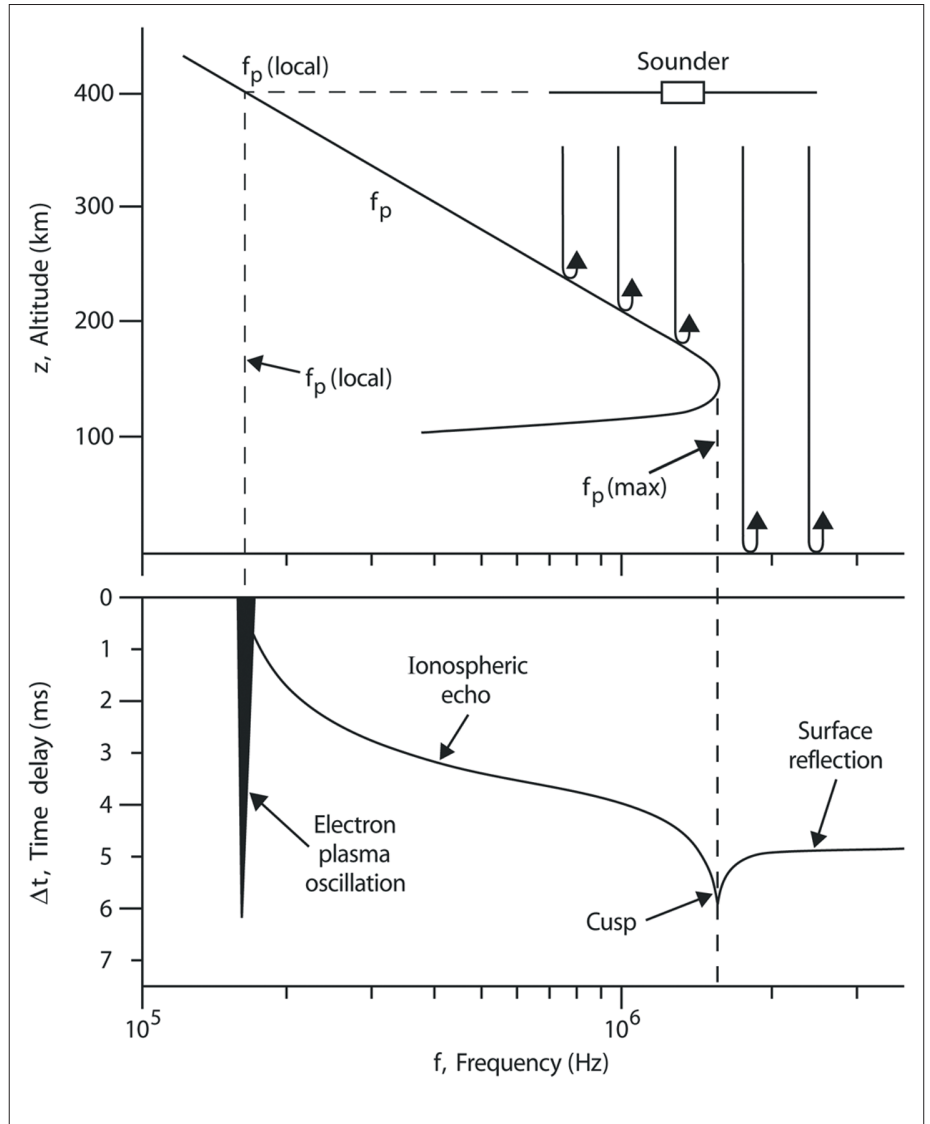
The extensive fields of yardangs in the MFF deposits, landforms that occur in variably indurated to poorly consolidated material that is easily eroded by wind, suggest that sublimation must have removed volatiles from the putative ice-rich deposits to leave metres of dust and sand. The accumulation of metres of sediments suggests that the non-ice component of an ice-rich MFF deposit may be larger than the maximum 10% estimated for the south polar layered deposits (Plaut et al., 2007). This, in turn, suggests a higher modelled real dielectric constant than that of pure ice. Although the real dielectric constant and dielectric losses may be consistent with an ice-rich material, the existing data do not exclude the possibility that the MFF deposits are an anomalously low density, ice-poor material. In either case, these deposits appear to have unique characteristics from other martian deposits studied to date by radar sounding. An ice-rich MFF raises the intriguing possibility of a large volume of water ice in the equatorial zone of Mars beneath a veneer of dust and sand. MARSIS observations suggest that the total volume of ice in the SPLD is $\sim 1.6 \times 10^6$ km³ (Plaut et al., 2007). If the MFF deposits are ice-rich, estimates of their total volume suggest a volume of water comparable to that in the SPLD.

6.1 Ionospheric Sounding Results

Spacecraft radar sounders were originally developed in the 1960s to study Earth's ionosphere (e.g. Franklin & Maclean, 1969) and have proven to be a powerful tool for studying ionospheric physics. Most of our knowledge of the martian ionosphere

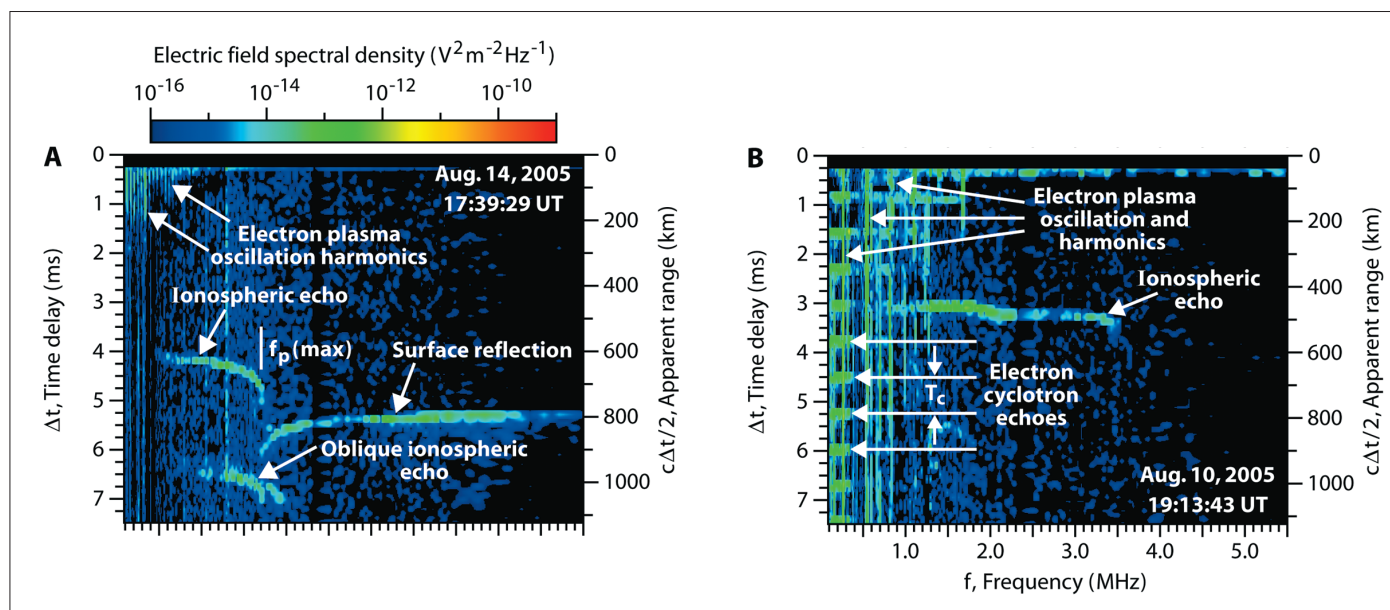
6. The Ionosphere

Fig. 10. The top panel shows a representative profile of the electron plasma frequency, f_p , in the martian ionosphere as a function of altitude, z , and the bottom panel shows the corresponding ionogram, which is a plot of the delay time, Δt , for a sounder pulse at a frequency f , to reflect and return to the spacecraft. The intense vertical 'spike' at the local electron plasma frequency, $f_p(\text{local})$ is caused by electron plasma oscillations excited by the sounder pulse. At frequencies from $f_p(\text{local})$ to the maximum frequency in the ionosphere, $f_p(\text{max})$, an ionospheric echo is detected, followed at higher frequencies by a reflection from the surface. The ionospheric echo trace and the surface reflection trace form a cusp centred on $f_p(\text{max})$.



comes from radio occultation measurements, which provide an average electron density along a line of sight from Earth to a spacecraft in orbit around Mars (Zhang et al., 1990; Pätzold et al., 2005). The MARSIS measurements nicely complement these measurements by providing better spatial resolution, and observations in regions where radio occultation measurements cannot be made. Due to geometric constraints imposed by the orbits of Earth and Mars, radio occultation measurements are restricted to solar zenith angles from about 48° to 132° .

A horizontally stratified ionosphere provides an almost perfectly reflecting surface for radio echo sounding. The reflection (Fig. 10) occurs because free-space electromagnetic radiation cannot propagate at frequencies below the electron plasma frequency (Gurnett & Bhattacharjee, 2005), which is given by $f_p = 8980 (n_e)^{1/2}$ Hz, where n_e is the electron number density in cm^{-3} . Echo time delays are measured as a function of frequency by sequentially stepping the transmission frequency over the frequency range of interest. Three types of echoes usually occur (Fig. 10). The first is a very strong 'spike' at the local electron plasma frequency, $f_p(\text{local})$. This response is caused by excitation of electrostatic oscillations at the electron plasma frequency. The second is an echo from the ionosphere that extends from $f_p(\text{local})$ to the maximum



plasma frequency in the ionosphere, $f_p(\text{max})$, above which the radio wave can penetrate through the ionosphere to the surface. The third is a surface reflection that extends from $f_p(\text{max})$ to the maximum sounding frequency. The ionospheric echo and the surface reflection come together in a sharply defined cusp, centred on $f_p(\text{max})$. The cusp occurs because the propagation speed of the wave packet (i.e. the group velocity) is very small over an increasingly long path length as the wave frequency approaches $f_p(\text{max})$.

The Mars Express spacecraft is in an eccentric orbit around Mars with a periapsis altitude of about 275 km, an apoapsis altitude of about 10 100 km, an orbital inclination of 86° , and a period of 6.75 hours. Because of gravitational perturbations the local time and latitude of periapsis evolve rather rapidly. The ionospheric soundings are typically displayed in the form of an ionogram, which is a plot of the echo strength versus frequency and time delay. Two ionograms (Fig. 11) have been selected to illustrate the range of phenomena typically observed. The closely spaced vertical lines in the upper left-hand corner of the first ionogram (Fig. 11a) are at harmonics of the local electron plasma frequency and are caused by the excitation of electron plasma oscillations, in this case at a frequency that is slightly below the low-frequency cutoff (100 kHz) of the receiver. Even though the fundamental of the plasma frequency is not observed directly in this case, the plasma frequency can still be determined from the spacing of the harmonics, and is $f_p(\text{local}) = 44$ kHz. At somewhat higher frequencies, from about 0.5 to 1.7 MHz, a strong well defined ionospheric echo can be seen with time delays ranging from about 4 to 5 ms. At even higher frequencies, from about 1.7 to 5.5 MHz, a strong reflected signal from the surface of Mars is apparent. The maximum plasma frequency in the ionosphere, $f_p(\text{max})$, can be identified from the cusp and is 1.71 MHz. An unexpected feature is the presence of a second ionospheric echo with time delays ranging from about 6.3 to 7.1 ms. This echo has to arise from an oblique reflection, since the apparent range ($c\Delta t/2$, where c is the speed of light) given on the right side of the spectrogram is substantially greater than the distance to either the ionosphere or the surface. The origin of such oblique echoes will be discussed later.

Another unexpected effect, consisting of a series of echoes equally spaced in time, is seen along the left-hand edge of a second ionogram (Fig. 11b). Comparisons of these echoes with the magnetic field model of Cain et al. (2003) show that the repetition rate of these echoes, $1/T_c$, is almost exactly the local electron cyclotron frequency,

Fig. 11. Two ionograms selected to illustrate typical features found in the MARSIS ionospheric soundings. The ionograms display echo strength (colour coded) as a function of frequency, f , and time delay, Δt , with time delay plotted positive downward along the vertical axis. The apparent range to the reflection point, $c\Delta t/2$, where c is the speed of light, is shown on the right. Ionogram (A) was obtained near the evening terminator at a solar zenith angle of $\chi = 89.3^\circ$ and an altitude of 778 km. Ionogram (B) was obtained on the dayside at a solar zenith angle of $\chi = 47.9^\circ$ and an altitude of 573 km. Electron plasma oscillation harmonics can be seen in both ionograms, as well as strong echoes from the ionosphere. Ionogram (B) has a series of horizontal, equally spaced echoes along the left-hand side. These echoes occur at the electron cyclotron period, and are called electron cyclotron echoes. They are believed to be caused by the cyclotron motion of electrons accelerated by the transmitter pulse. Although a strong surface reflection is present in (A), note that no surface reflection is present in (B). Surface reflections are seldom seen at solar zenith angles less than about 40° or during periods of intense solar activity.

$f_c = 28 B$ Hz, where B is the magnetic field strength (in nT). Because of the close relationship to the electron cyclotron frequency, these echoes are called ‘electron cyclotron echoes’. Such echoes are very common and are usually present whenever the magnetic field strength is greater than a few tens of nT. We believe that these echoes are caused by electrons accelerated by the strong electric fields near the antenna during each cycle of the transmitter waveform. The cyclotron motion of the electrons in the local magnetic field then causes these electrons to periodically return to the vicinity of the antenna where they induce a signal on the antenna. For this process to occur, the magnetic field strength must be reasonably uniform over a spatial region comparable to the cyclotron radius. For a magnetic field strength of 100 nT, which is a typical crustal field strength at the spacecraft, and a voltage of 500 V, which is the typical antenna voltage, the cyclotron radius is about 1 km. Since the crustal magnetic fields have scale sizes of hundreds of kilometres, this condition is easily satisfied.

In contrast to the first ionogram (Fig. 11a), no surface reflection can be detected in the second ionogram (Fig. 11b). The intensity of the surface reflection is found to be highly variable, a topic of considerable importance for subsurface sounding. Some of this variability can be attributed to solar activity. For example, surface reflections disappeared completely about two days after a class X17 solar flare that occurred on 7 September 2005, and did not reappear until 23 September, nearly two weeks later. Although further analysis is needed, it seems almost certain that the absorption is caused by energetic charged particles produced by solar flares. The onset of the absorption is usually delayed by a day or more after a flare and tends to last many days, much longer than the typical time scale for decay of the ultraviolet and X-ray radiation associated with a flare. At Earth it is well known that energetic protons from solar flares cause enhanced ionisation and absorption of radio waves in the lower levels of the ionosphere, and a similar process may occur at Mars. In addition to the solar flare control, the absorption also appears to increase with decreasing solar zenith angle. Even during periods of low solar activity surface reflections are rarely observed when the solar zenith angle is less than about 40° .

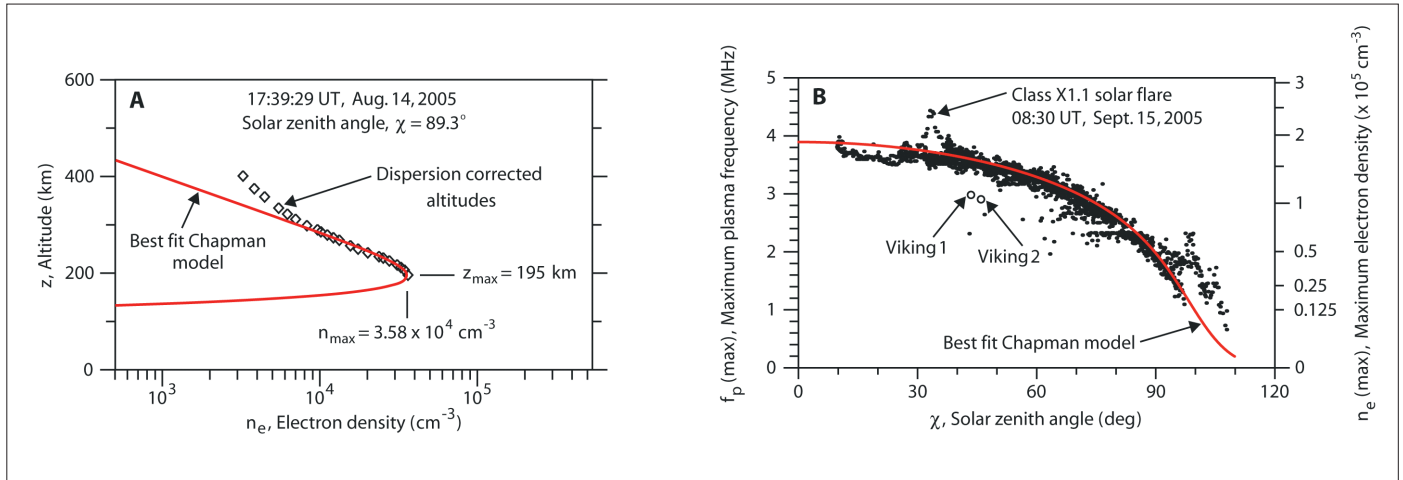
6.2 Ionospheric Density Models

In order to compare the MARSIS ionospheric soundings with various ionospheric models, it is necessary to convert the soundings to usable electron density profiles. Although a rough estimate of the density profile can be obtained from the apparent range to the reflection point, for accurate measurements it is necessary to correct for dispersion, which is the effect the plasma has on the propagation speed of the wave. For vertical incidence on a horizontally stratified ionosphere the round-trip delay time as a function of frequency, $\Delta t(f)$, is given by the integral

$$\Delta t(f) = \frac{2}{c} \int_{z(f_p)}^{z_{sc}} \frac{dz}{\sqrt{1 - \frac{f_p^2(z)}{f^2}}} \quad (1)$$

where the integration is carried out from the reflection point altitude, $z(f_p)$, to the spacecraft altitude, z_{sc} . Since $\Delta t(f)$ is known from the ionospheric echo trace, the basic problem is to invert the integral to obtain $z(f_p)$, i.e. the altitude of the reflection point as a function of the plasma frequency. Once this is known, the equation $f_p = 8980 (n_e)^{1/2}$, can be used to obtain $z(n_e)$.

Although the mathematical techniques for carrying out this inversion are straightforward, there are sometimes practical difficulties. For example, the ionospheric echo trace often does not extend down to the local plasma frequency (Fig. 11). In such cases it is necessary to make a reasonable guess as to how the echo trace extends from the lowest frequency measured to the local plasma frequency. Normally the inversion is not very sensitive to this choice, since the correction to the propagation speed becomes quite small when the plasma frequency is well below the wave frequency.



An example of an electron density profile obtained by inverting eq. (1) is shown in Fig. 12(a). This profile was obtained by using both the ionospheric echo trace and the surface reflection trace (Fig. 11a). Our approach was to select a theoretical model for the density profile and then adjust the parameters in the model to give the overall best fit to the measured time delays. For a density model we use the following equation from Chapman (1931):

$$n_e = n_0 \exp \left[\frac{1}{2} \left\{ 1 - \frac{z - z_0}{H} - \text{Ch}(x, \chi) \exp \left(-\frac{z - z_0}{H} \right) \right\} \right] \quad (2)$$

where z is the altitude, n_0 is the maximum electron density at the subsolar point, and z_0 is the altitude of this maximum. The function $\text{Ch}(x, \chi)$ is called Chapman's grazing incidence function and takes into account the absorption of the solar radiation as it passes obliquely through the atmosphere. This function depends on the solar zenith angle, χ , and a dimensionless parameter $x = (R_M + z_0)/H$, where $R_M = 3396$ km is the radius of Mars, and H is the scale height of the neutral atmosphere. $\text{Ch}(x, \chi)$ can be computed from a power series (Chapman, 1931), or from a table provided by Wilkes (1954). The fit to the top-side electron density profile is very good (Fig. 7A). The maximum electron density, $n_{\max} = 3.58 \times 10^4 \text{ cm}^{-3}$, and the altitude of the maximum, $z_{\max} = 195$ km, are in reasonable agreement with radio occultation results at this solar zenith angle (Zhang et al., 1990). Although the bottom-side electron density profile cannot be expected to represent complicated features, such as multiple density layers, the model does accurately represent the top-side electron density profile near the peak, and the total electron content (TEC) through the ionosphere, which is determined by the dispersion of the surface reflection. The total electron content is defined as the integral $\int n_e dz$ along a vertical line through the ionosphere and, in this case, is $\text{TEC} = 3.7 \times 10^{11} \text{ cm}^{-2}$. The deviation of the measured electron densities from the model at altitudes above about 300 km is probably caused by upward diffusion of plasma away from the region of photochemical equilibrium described by Chapman's model.

To study the dependence of the maximum electron density, n_{\max} , on the solar zenith angle, χ , the maximum frequencies of the ionospheric echo traces have been measured for 12 randomly selected passes from 5 July to 10 October 2005. During this time the solar zenith angle at periapsis systematically decreased from 98° to 16° , thereby providing a good sampling of solar zenith angles. A scatter plot of the measured $f_p(\max)$ values is shown in Fig. 12(b) as a function of solar zenith angle. As can be seen, the maximum plasma frequency has a very clear systematic dependence on solar zenith angle, varying from about 3.9 MHz near the subsolar point to less than 1 MHz

Fig. 12. Two illustrations comparing electron densities obtained from ionospheric soundings to the Chapman (1931) ionospheric density model. The diamond-shaped points in (A) give the electron density profile computed from the ionospheric echo trace in Fig. 6A after correcting for dispersion. The red curve gives the best fit to this density profile, while simultaneously providing a good fit to the surface reflection trace. The best fit parameters are $1.32 \times 10^5 \text{ cm}^{-3}$, 130 km, $z_{\max} = 195$ km, $n_{\max} = 3.58 \times 10^4 \text{ cm}^{-3}$, $H = 25$ km, $x = 141$, and $\text{Ch}(x, \chi) = 13.5$. Plot (B) shows the maximum plasma frequency in the ionosphere, $f_p(\max)$, as a function of solar zenith angle, χ , for 12 randomly selected orbits. The corresponding electron density is shown on the right side of the plot. The red line is the best fit to the Chapman electron density model using $(q_0/a)1/2 = 1.98 \times 10^5 \text{ cm}^{-3}$.

on the nightside. A scale showing the corresponding electron density values is given on the right-hand side of the plot. These electron densities are in good agreement with the results from radio occultation measurements (Zhang et al., 1990), but are slightly higher than the *in situ* Viking 1 and 2 measurements (Hanson et al., 1977), which were obtained during a less active phase of the solar cycle.

The solar zenith angle dependence (Fig. 12b) can be compared directly with the predictions of Chapman's electron density model. In Chapman's model, the maximum electron density in the ionosphere is given by

$$n_e(\text{max}) = (q_0/\alpha)^{1/2} / \text{Ch}(x, \chi)^{1/2} \quad (3)$$

where q_0 is the ionisation rate at the subsolar point, and α is the recombination rate. The best fit of this equation to the measured $n_e(\text{max})$ values is shown by the red line. This fit uses the same basic parameters as in the first fit (Fig. 12a), with the exception of the parameter $(q_0/\alpha)^{1/2} = 1.98 \times 10^5 \text{ cm}^{-3}$, which has been adjusted to give the best overall fit. The fit has been purposely selected near the densest cluster of points, ignoring the outlying points. The outlying points are almost certainly influenced by solar events. For example, the sharp peak in the density that occurred during a pass at a solar zenith angle of about 34° coincides with a class X1.1 solar flare that occurred at 08:30 UT (Universal Time) on 15 September 2005. The enhanced electron densities during this event are almost certainly caused by an intense burst of ultraviolet radiation arriving from the Sun. Other large enhancements, well above the electron densities predicted by Chapman's equation, can also be seen on the nightside at solar zenith angles of 98° and 104° .

These events are not associated with any known solar flare activity. The ionospheric echoes in this region are often very diffuse and sometimes have unusual characteristics, such as a surface reflection that extends below the ionospheric echo trace. Such echoes are impossible in a horizontally stratified ionosphere and are suggestive of considerable small-scale structure, possibly consisting of low-density 'holes,' like those observed on the nightside of Venus (Brace et al., 1982).

7. Oblique Echoes

Oblique ionospheric echoes (Fig. 11a) are a common feature in the MARSIS ionograms. Inspection of successive ionograms shows that the range of these echoes systematically either increases or decreases with increasing time and sometimes merges with the vertical echoes. A good way to study these echoes is to make a plot of the echo strength at a fixed frequency as a function of time and apparent altitude (Fig. 13). Apparent altitude is defined as the spacecraft altitude minus the apparent range. In this display the vertical echo is the nearly horizontal line at an altitude of about 120 km. The oblique echoes almost always have the shape of a downward-facing hyperbola, sometimes consisting of both branches, but more frequently consisting of only one branch or part of a branch. Sometimes the apex of the hyperbola merges with the vertical echo, as in the event marked A. In a radar display of this type, hyperbola-shaped echoes are characteristic of relative motion between the radar and an off-vertical target.

The asymptotic slopes of the hyperbola-shaped echoes are consistent with the motion of the spacecraft relative to a feature that is fixed with respect to Mars. We have verified this hypothesis by comparing repeated passes over the same region of Mars. Such comparisons show that nearly identical hyperbola-shaped features often reappear over the same region. The ones that do not show a good pass-to-pass correlation often occur in very complicated regions with many overlapping echoes, such as that near the centre of Fig. 13.

Strong evidence exists that most of the oblique ionospheric echoes are related to ionospheric density structures caused by the crustal magnetic fields discovered by the Mars Global Surveyor spacecraft (Acuña et al., 1998, 1999). In a comparison (bottom panel of Fig. 13) with the crustal magnetic field computed at an altitude of 150 km using the global magnetic field model developed by Cain et al. (2003), the oblique

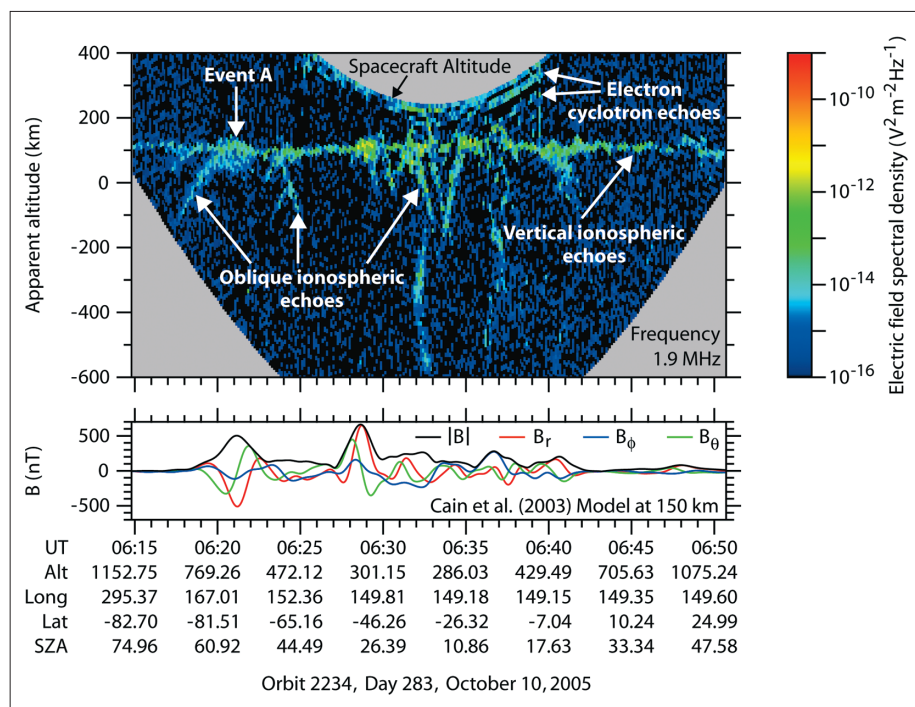


Fig. 13. The top panel shows echo strengths at a frequency of 1.9 MHz plotted as a function of time and apparent altitude, which is the spacecraft altitude minus the apparent range of the echo. The bottom panel shows three components, B_r , B_θ , and B_ϕ , of the crustal magnetic field and the magnitude of the magnetic field, $*B^*$, computed from the model of Cain et al. (2003) at an altitude of 150 km. The nearly horizontal echoes at an altitude of about 120 km are vertical echoes, and the downward-facing hyperbola-shaped features are oblique echoes. This and other similar examples provide strong evidence that density structures related to crustal magnetic fields are responsible for most of the oblique echoes.

echoes are seen to occur in the region where strong magnetic fields are present. Inspection of other similar plots confirm this basic relationship

Although the detailed correlation between the oblique echoes and the magnetic field is often complicated and difficult to resolve, in some cases, such as event A in Fig. 13, the relationship is quite clear. For this event the apex of the hyperbola-shaped echo is coincident with a well defined peak in the magnetic field. Furthermore, near the apex, the altitude of the oblique echo (which has merged with the vertical echo) is clearly seen to be greater than the altitude of the surrounding ionosphere, which indicates an upward bulge in the ionosphere. Note also that the magnetic field is nearly vertical in this region, as can be seen by the radial (vertical) component, B_r , which is much stronger than either the southward, B_θ , or eastward, B_ϕ , components. These and numerous other similar observations lead us to conclude that the oblique echoes usually arise from an upward bulge in the ionosphere in a region where the magnetic field is nearly vertical (Fig. 14a). As the spacecraft approaches the bulge, oblique echoes start as soon as the constant density surface ($f = f_p$) is normal to the line-of-sight from the spacecraft (Fig. 14b). Two echoes are then detected until the spacecraft is nearly over the bulge, at which point the vertical echo disappears or merges with the oblique echo as the spacecraft passes over the bulge. This basic model is consistent with radar occultation measurements that show an increase in the scale height in regions where the crustal magnetic field is nearly vertical (Krymskii et al., 2002). The bulge is believed to be due to heating, and the resulting increase in the scale height, caused by solar wind electrons that have access to the lower levels of the ionosphere along open magnetic field lines. More complex structures probably exist in regions where the magnetic field is very complex, such as near the middle of the plot in Fig. 13, or in regions where the crustal magnetic fields are strong enough to stand off the solar wind (Mitchell et al., 2001).

Although crustal magnetic fields are almost certainly involved in producing the majority of the oblique echoes, cases have been found where the echoes exist in regions where the model of Cain et al. (2003) does not predict significant crustal magnetic fields. We do not know if these cases involve a failure of the model, or whether there are other

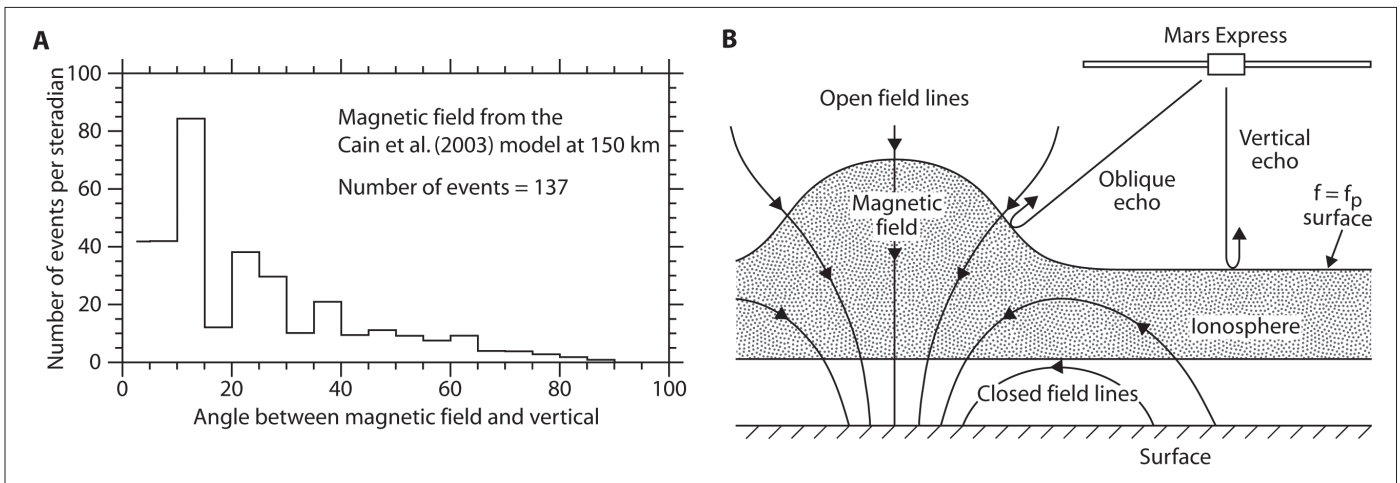


Fig. 14. Panel (A) shows the distribution of oblique echo events as a function of the angle between the magnetic field and vertical. The angles were evaluated at the apex of the hyperbola-shaped time delay feature using the model of Cain et al. (2003). Most of the events occur at angles less than about 40°E, indicating that the density structures responsible for the oblique echoes tend to occur in regions where the magnetic field is nearly vertical. Panel (B) shows a sketch of the ionospheric density structures that are thought to be responsible for the oblique ionospheric

echoes. As the spacecraft approaches the bulge in the ionosphere the sounder detects two echoes, a vertical echo from the ionosphere and an oblique echo from the bulge. As the spacecraft passes over the bulge, the vertical echo either merges with the oblique echo or disappears entirely, depending on the exact shape of the bulge. The bulge in the ionosphere is believed to be due to ionospheric heating caused by hot solar wind electrons that reach the lower levels of the ionosphere along open magnetic field lines.

mechanisms for producing such echoes. Possible mechanisms that we intend to consider are wind-driven atmospheric waves excited by topographic features and various types of wave-like structures in the ionosphere driven by interactions with the solar wind.

8. Discussion and Conclusions

MARSIS has demonstrated a capability to detect structures and layers in the subsurface of Mars that are not detectable by other sensors, past or present. The low attenuation observed in the polar layered deposits (PLD) indicates a composition of nearly pure, cold water ice. The lack of a significant deflection of the plains surface below the PLD implies a very thick elastic lithosphere in these regions. The detection of deep interfaces with minimal loss in the equatorial Medusae Fossae formation indicates a low material density, and suggests the possibility of a large reservoir of ice away from the poles.

The MARSIS ionospheric soundings have shown that the ionosphere of Mars is in good agreement with the expectations of Chapman's 1931 photo-equilibrium theory for origin of planetary ionospheres. The soundings have also revealed a number of unexpected features. These include echoes that reoccur at the electron cyclotron period, large variations in the absorption apparently caused by energetic solar events, oblique echoes caused by ionospheric structures associated with the crustal magnetic fields of Mars, diffuse echoes apparently caused by scattering from ionospheric irregularities, and ionospheric holes. Since the subsurface soundings must occur at frequencies well above the maximum electron plasma frequency in the ionosphere and under conditions of low ionospheric absorption, these measurements have already proved to be quite useful for planning subsurface sounding operations. The electron cyclotron echoes also provide a new method of measuring the local magnetic field strength, which is useful since Mars Express does not have a magnetometer.

Note: Much of the material in this paper has been published in the journals *Science* and *Nature*; see Picardi et al. (2005), Plaut et al. (2007), Watters et al. (2007) and Gurnett et al. (2005).

References

- Acuña, M.H., J.E.P. Connerney, P. Wasilewski, R.P. Lin, K.A. Anderson, C.W. Carlson, J. McFadden, D.W. Curtis, D. Mitchell, H. Rème, C. Mazelle, J.A. Sauvaud, C. d'Uston, A. Cros, J.L. Medale, S.J. Bauer, P. Cloutier, M. Mayhew, D. Winterhalter & N.F. Ness (1998). Magnetic Field and Plasma Observations at Mars: Initial Results of the Mars Global Surveyor Mission, *Science* **279**, 167.
- Acuña, M.H., J.E.P. Connerney, N.F. Ness, R.P. Lin, D. Mitchell, C.W. Carlson, J. McFadden, K.A. Anderson, H. Rème, C. Mazelle, D. Vignes, P. Wasilewski & P. Cloutier (1999). Global Distribution of Crustal Magnetization Discovered by the Mars Global Surveyor MAG/ER Experiment. *Science* **284**, 790.
- Brace, L., R. Theis, H. Mayr, S. Curtis & J. Luhmann (1982). Holes in the Nightside Ionosphere of Venus. *J. Geophys. Res.* **87**, 199.
- Bradley, B.A., S.E.H. Sakimoto, H. Frey & J.R. Zimbelman (2002). Medusae Fossae Formation: New Perspectives from Mars Global Surveyor. *J. Geophys. Res.* **107**, 5058.
- Byrne, S. & Ingersoll, A.P. (2003). A Sublimation Model for Martian South Polar Ice Features. *Science* **299**, 1051. DOI: 10.1126/science.1080148.
- Byrne, S. & Murray, B.C. (2002). North Polar Stratigraphy and the Paleo-erg of Mars. *J. Geophys. Res.* **107**(E6), 5044. DOI : 10.1029/2001JE001615.
- Cain J. C., B.B. Ferguson & D. Mozzoni (2003). An $n = 90$ Internal Potential Function of the Martian Crustal Magnetic Field. *J. Geophys. Res.* **108**, 5008.
- Carrier, W.D., G.R. Olhoeft & W. Mendell (1991), in *Lunar Sourcebook*. Cambridge University Press, New York, pp. 475–594.
- Franklin, C.A. & M.A. Maclean (1969). The Design of Swept-frequency Topside Sounders. *Proc. IEEE* **57**, 897.
- Greeley, R. & J.E. Guest (1987). *US Geol. Surv. Misc. Invest. Ser. Map*, I-1802-B.
- Gurnett, D.A. & A. Bhattacharjee (2005). *Introduction to Plasma Physics*. Cambridge University Press, Cambridge, p.114.
- Gurnett, D.A., Kirchner, D.L., Huff, R.L., Morgan, D.D., Persoon, A.M., Averkamp, T.F., Duru, F., Nielsen, E., Safaeinili, A., Plaut, J.J. & Picardi, G. (2005). Radar Soundings of the Ionosphere of Mars, *Science* **310**, 1929–1933.
- Hanson, W.B., S. Sanatani & D.R. Zuccaro (1977). The Martian Ionosphere as Observed by the Viking Retarding Potential Analyzers. *J. Geophys. Res.* **82**, 4351.
- Head, J.W. & M. Kreslavsky (2004). Medusae Fossae Formation: Ice-rich Airborne Dust Deposited during Periods of High Obliquity? *Lunar Planet. Sci.* **35**, 1635 (abstract).
- Hynek, B.M., R.J. Phillips, R.E. Arvidson (2003). Explosive Volcanism in the Tharsis Region: Global Evidence in the Martian Geologic Record, *J. Geophys. Res.* **108**, 5111.
- Krymskii A.M., T.K. Breus, N.F. Ness, M.H. Acuña, J.E.P. Connerney, D.H. Crider, D.L. Mitchell & S.J. Bauer (2002). Structure of the Magnetic Field Fluxes Connected with Crustal Magnetization and Topside Ionosphere at Mars. *J. Geophys. Res.* **107**, 1245.
- Lanagan, P., A. McEwen, L. Keszthelyi, and T. Thordarson (2001). Rootless Cones on Mars Indicating the Presence of Shallow Equatorial Ground Ice in Recent Times, *Geophys. Res. Lett.*, **28**(12), 2365-2367
- Mitchell, D., R. Lin, C. Mazelle, H. Rème, P. Cloutier, J. Connerney, M. Acuna & N. Ness (2001). Probing Mars' Crustal Magnetic Field and Ionosphere with the MGS Electron Reflectometer. *J. Geophys. Res.* **106**, 23419.
- Muhleman, D.O., B.J. Butler, A.W. Grossman & M.A. Slade (1991). Radar Images of Mars. *Science* **253**, 1508.
- Nouvel, J.-F., Herique, A., Kofman, W. & Safaeinili, A. (2004). Radar Signal Simulation: Surface Modeling with the Facet Method, *Radio Sci.* **39**, RS1013. DOI: 10.1029/2003RS002903.
- Pätzold, M., S. Tellmann, B. Häusler, D. Hinson, R. Schaa & G. L. Tyler (2005). A Sporadic Third Layer in the Ionosphere of Mars, *Science* **310**, 837.
- Picardi, G., Biccari, D., Seu, R., Plaut, J.J., Johnson, W.T.K., Jordan, R.L., Safaeinili, A., Gurnett, D.A., Huff, R., Orosei, R., Bombaci, O., Calabrese, D. & Zampolini, E. (2004). MARSIS: Mars Advanced Radar for Subsurface and Ionosphere Sounding, in *Mars Express: The Scientific Payload*, ESA SP-1240, ESA Publications Division, European Space Agency, Noordwijk, the Netherlands, pp.51–69.

- Picardi, G., Plaut, J.J., Biccari, D., Bombaci, O., Calabrese, D., Cartacci, M., Cicchetti, A., Clifford, S.M., Edenhofer, P., Farrell, W.M., Federico, C., Frigeri, A., Gurnett, D.A., Hagfors, T., Heggy, E., Herique, A., Huff, R.L., Ivanov, A.B., Johnson, W.T.K., Jordan, R.L., Kirchner, D.L., Kofman, W., Leuschen, C.J., Nielsen, E., Orosei, R., Pettinelli, E., Phillips, R.J., Plettemeier, D., Safaeinili, A., Seu, R., Stofan, E.R., Vannaroni, G., Watters, T.R. & Zampolini, E. (2005). Radar Soundings of the Subsurface of Mars, *Science* **310**, 1925–1928.
- Plaut, J.J., Picardi, G., Safaeinili, A., Ivanov, A.B., Milkovich, S.M., Cicchetti, A., Kofman, W., Mouginot, J., Farrell, W.M., Phillips, R.J., Clifford, S.M., Frigeri, A., Orosei, R., Federico, C., Williams, I.P., Gurnett, D.A., Nielsen, E., Hagfors, T., Heggy, E., Stofan, E.R., Plettemeier, D., Watters, T.R., Leuschen, C.J. & Edenhofer, P. (2007). Subsurface Radar Sounding of the South Polar Layered Deposits of Mars, *Science* **315**, 92–95, DOI: 10.1126/science.1139672.
- Porcello, L.J., R.L. Jordan, J.S. Zelenka, G.F. Adams, R.J. Phillips, W.E. Brown, S.H. Ward, & P.L. Jackson (1974). The Apollo Lunar Sounder Radar System. *Proc. IEEE* **62**, 769.
- Safaeinili, A., W. Kofman, J.-F. Nouvel, A. Herique, & R.L. Jordan, R.L. (2003). Impact of Mars Ionosphere on Orbital Radar Sounder Operation and Data Processing, *Planet. Space Sci.* **51**, 505.
- Sakimoto, S.E.H., H.V. Frey, J. B. Garvin & J. H. Roark (1999). Topography, Roughness, Layering, and Slope Properties of the Medusae Fossae Formation from Mars Orbiter Laser Altimeter (MOLA) and Mars Orbiter Camera (MOC) data. *J. Geophys. Res.* **104**, 24141.
- Schultz, P.H. & A.B. Lutz (1988). Polar Wander of Mars. *Icarus* **73**, 91.
- Scott, D.H. & K.L. Tanaka (1986). *US Geol. Surv. Misc. Invest. Ser. Map*, I-1802-A.
- Smith, D.E., Zuber, M.T., Solomon, S.C., Phillips, R.J., Head, J.W., Garvin, J.B., Banerdt, W.B., Muhleman, D.O., Pettengill, G.H., Neumann, G.A., Lemoine, F.G., Abshire, J.B., Aharonson, O., Brown, C.D., Hauck, S.A., Ivanov, A.B., McGovern, P.J., Zwally, H.J. & Duxbury, T.C. (1999). The Global Topography of Mars and Implications for Surface Evolution, *Science* **284**, 1495.
- Tanaka, K. & E. Kolb (2005). Geologic Mapping of the Polar Regions of Mars: Preliminary Results and Climate Implications. *US Geol. Surv. Open File Rept.* 2005-1271.
- Thomas, P.C., Squyres, S., Herkenhoff, K., Howard, A. & Murray, B. (1992) in *Mars* (Eds. H.H. Kieffer et al.), University of Arizona Press, Tucson, pp.767–795.
- Watters, T.R., Campbell, B.A., Carter, L., Leuschen, C.J., Plaut, J.J., Picardi, G., Safaeinili, A., Clifford, S.M., Farrell, W.M., Ivanov, A.B., Phillips, R.J. & Stofan, E.R. (2007). Radar Sounding of the Medusae Fossae Formation Mars: Equatorial Ice or Dry, Low-Density Deposits? *Science* **318**, 112. DOI: 10.1126/science.1148112.
- Wilkes, M.V. (1954). A Table of Chapman's Grazing Incidence Integral $Ch(x, \chi)$. *Proc. R. Soc. B* **67**, 304.
- Zhang, M.H.G., J.G. Luhmann & A.J. Kliore (1990). An Observational Study of the Nightside Ionospheres of Mars and Venus with Radio Occultation Methods. *J. Geophys. Res.* **95**, 17095.
- Zimbelman, J. et al. (1999). Medusae Fossae Formation, Mars: An Assessment of Possible Origins Utilizing Early Results from Mars Global Surveyor. *Lunar Planet. Sci.* **30**, 1652 (abstr.)